Mixing Matters: Nanoscale Heterogeneity and Stability in Metal Halide Perovskite Solar Cells

Laura E. Mundt^{1,*}, Fei Zhang^{2,3}, Axel F. Palmstrom², Junwei Xu¹, Robert Tirawat², Leah L. Kelly¹, Kevin H. Stone¹, Kai Zhu², Joseph J. Berry², Michael F. Toney^{1,4,5,*}, Laura T. Schelhas^{1,2,*}

¹SLAC National Accelerator Laboratory, 2575 Sand Hill Rd, Menlo Park, CA 94025, USA

²National Renewable Energy Laboratory, 15013 Denver W Pkwy, Golden, CO 80401, USA

³School of Chemical Engineering and Technology, Tianjin University, Tianjin, 300072, China

⁴Department of Chemical and Biological Engineering, University of Colorado Boulder, Boulder, CO 80303, USA

⁵Renewable and Sustainable Energy Institute (RASEI), University of Colorado Boulder, Boulder, CO 80303, USA

AUTHOR INFORMATION

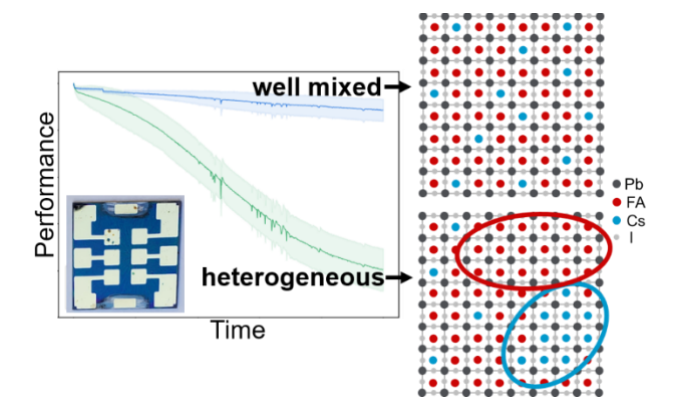
Corresponding Author

*Laura E. Mundt (lmundt@slac.stanford.edu), Michael F. Toney (michael.toney@colorado.edu), Laura T. Schelhas (laura.schelhas@nrel.gov)

ABSTRACT

The structural stability of the metal halide perovskite (MHP) absorber material is crucial for the long term solar cell stability in this thin-film photovoltaic technology. Here, we use mixed A-site FA_{0.83}Cs_{0.17}PbI₃ to demonstrate that nanoscale compositional heterogeneity can serve as initiation sites for more macroscale, irreversible phase segregation which causes device performance degradation. Probing compositional heterogeneity on length scales that has not been detected with conventional characterization techniques, we analyze the tetragonal to cubic phase transition behavior to indirectly determine the level of nanoscale compositional heterogeneity in the initial films. Further, we show that the thermal annealing conditions of the MHP layer during film processing influence the initial nanoscale compositional heterogeneity and changing these processing conditions can be used to improve the device performance stability. The insights into structural degradation mechanisms initiated by nanoscale compositional heterogeneity and the proposed mitigation strategies will help guide the way towards long term stable MHP solar cells.

TOC GRAPHICS



Metal halide perovskites (MHPs) are the most promising candidate for a high-efficiency, lightweight and cost-efficient thin film solar cell technology. With over ten years of intensive research, perovskite photovoltaics have reached efficiencies of over 25.5% for single junction devices and over 29.8% in tandem configurations with silicon¹. One appealing property of MHPs is their ability to accommodate ions of different sizes into the crystal lattice, tuning the size of the lattice and thereby controlling optoelectronic properties such as the band gap^{2–7}. The highest performing MHP solar cells, including the previously mentioned efficiency records, were achieved for mixed ionic systems. That means multiple ions of different sizes occupy the A-, B- or X-sites in the perovskite ABX₃ lattice. These alloy-like materials not only enable tuning of the band gap across a wide range, but also offer superior structural stability compared to pure phase compositions like MAPbI₃, FAPbI₃ or CsPbI₃^{8–15}.

An important and well-established tool to predict structural stability in perovskites is the Goldschmidt tolerance factor $t_G^{11,16}$. The tolerance factor is the ratio of the ionic radii and is a measure for the ability to maintain the perovskite crystal structure. For example, the mixed A-site cation perovskite $FA_{1-x}Cs_xPbI_3$ (FA = formamidinium) has a tolerance factor closer to the optimal range of 0.9 - 1 compared to the two single A-site compositions themselves¹¹. This is consistent with numerous observations of the superior stability of the mixed system. However, the tolerance factor is not all-encompassing and not always sufficient to predict structural stability^{15,17–23}. Even with a suitable tolerance factor, mixed composition MHPs can thermodynamically phase segregate into FA- and Cs-rich areas and then transition into their non-photoactive δ -phases^{15,17,18,24–26}.

It is well established that heterogeneity in MHPs exists across multiple orders of magnitude in size^{27–32} and it has been suggested that initial compositional heterogeneity can further drive demixing and A-site or halide segregation during illumination^{33–38}. Compositional heterogeneity

refers to isolated pockets of 10-100 nm size of compositional distinct regions³⁹, deviating from the average/targeted perovskite composition in the film (e.g. regions with more or less FA/Cs). These pockets are likely ubiquitous through the film, a schematic illustration is shown in Figure S1. Local compositional heterogeneity in the A-site cation was explicitly found to be one cause for halide segregation after exposure to light²⁰. However, also in single-halide FA_{1-x}Cs_xPbI₃ perovskites, demixing and A-site segregation during operation was found to be a main cause for performance loss^{17,18}. Evidence found by thermodynamic calculations suggested that the observed de-mixing was driven by initial compositional heterogeneity on the micrometer range¹⁷. While characterization techniques for measuring compositional heterogeneities at the micrometer length scale are well established and widely used to study MHPs⁴⁰, probing these materials on shorter nanometer scales has proven challenging. With their soft lattice, MHPs can quickly change/ degrade under the external stimulus of probes used in nanoscale measurements. Chemical analyses on the nanometer length scale, such as X-ray fluorescence (XRF) and energy-dispersive X-ray spectroscopy (EDS), have been used to study the local composition and ion distribution. However, the samples have been prone to beam damage and the detected local clusters of varying compositions were on the micrometer scale and large enough to show up in X-ray diffraction (XRD) measurements as secondary phases 18,40-42. This still leaves the question of the potentially detrimental effect of heterogeneities on shorter length scales, which cannot be detected with widely used characterization techniques such as X-ray diffraction (XRD), micro-photoluminescence mapping or time-of-flight secondary ion mass spectroscopy (ToF-SIMS). Recently, photoemission electron microscopy (PEEM) has successfully been used to analyze grain boundaries and local defects and the technique will likely provide further crucial insights into defects and heterogeneity on small length scales near the surface^{43,44}. Additionally, complex measurement techniques such

as nano-infrared spectroscopy^{45,46} and scanning probe microscopy^{47,48} is used to characterize compositional heterogeneity in MHPs on the nanoscale. However, beyond the question of detection, it remains to be explored how to tune or mitigate compositional nanoscale heterogeneity.

In recent work by Barrier et al., the team demonstrated an X-ray scattering based method to characterize small length scale compositional heterogeneity³⁹. They show that nanoscale compositional heterogeneity manifests in broadening of the tetragonal to cubic phase transition. In their study, they compare pure perovskite compositions, MAPbI₃ and MAPbBr₃, to mixed compositions, FA_{1-x}Cs_xPb(I_{1-y}Br_y)₃. The basis of their approach relies on the observation that the reversible tetragonal to cubic phase transition temperature is a function of perovskite composition, therefore a system with a distribution of compositions (FA:Cs, Br:I) will result in an superposition of multiple phase transition temperatures and as a smeared tetragonal to cubic phase transition when averaging over the probed volume. Simply put, well-mixed systems should present a sharp phase transition over a small temperature range, whereas a poorly mixed system will transition over a wider window, providing an indirect measure for the nanoscale compositional heterogeneity. Therefore, the nanoscale compositional heterogeneity can indirectly be measured through a simple in situ scattering experiment examining the tetragonal to cubic phase transition, compatible with even lab scale diffractometers, making this quantification easily accessible.

Leveraging these recent findings, we conducted a thorough and systematic study to investigate initial nanoscale compositional heterogeneity in mixed MHPs synthesized with different annealing conditions and its correlation to device stability. We postulate that initial nanoscale compositional heterogeneity, and consequently device instabilities caused by operationally induced A-site segregation, can be mitigated by tuning the synthesis thermal annealing conditions. In order to test

our hypothesis, we carefully characterize the initial nanoscale compositional heterogeneity, based on the method presented by Barrier et al., in a set of MHP thin film samples annealed at different temperatures and times. Subsequently, we conduct in situ wide angle X-ray scattering (WAXS) experiments to measure the tetragonal to cubic phase transition behavior on these annealed films. We chose the mixed A-site cation system FA_{1-x}Cs_xPbI₃ to separate the effects of halide vs. the A-site cation segregation. More specifically, we selected a 17% Cs composition for its established performance and stability in PV devices^{3,49,50}. Device stability data over 1000 hours is presented along with synchrotron X-ray diffraction data of the degraded devices, establishing the structure-function relationship between the loss in device performance and irreversible compositional demixing initiated by initial nanoscale compositional heterogeneity. Confirming our hypothesis, we find that well-mixed systems show superior device stability and that performance loss is related to de-mixing. Thus, these results show that the processing conditions determine the initial heterogeneity of the active layer and thereby provide a key to enabling the synthesis of stable high efficiency MHP cells and modules.

EXPERIMENTAL APPROACH

In order to understand the influence of thermal annealing conditions on initial nanoscale compositional heterogeneity and the resulting device performance stability, we combine thorough structural characterization with device stability testing. For simplicity, we will use the term "nanoscale heterogeneity" for the nanoscale compositional heterogeneity in the MHP thin films after deposition and subsequent annealing. We analyze fully annealed FA_{0.83}Cs_{0.17}PbI₃ thin films and full devices where the perovskite absorber layer was processed with differing annealing conditions after spin coating, summarized in Table 1, to intentionally vary nanoscale compositional heterogeneity across the samples. The remainder of the device and film stacks are

processed identically. The films and devices were prepared using previously published methods and more details can be found in the methods section. We vary both the annealing temperature (Ta), ranging from 100°C to 180°C, and the annealing time (ta), ranging from 15 min to 90 min. Throughout the manuscript we will refer to samples using "Ta-ta" format. For example a sample annealed at 100°C for 15 min will be noted as "100-15". We systematically investigate how the thermal annealing conditions influence heterogeneity and performance stability in fully annealed films and devices. To analyze the performance stability, we prepared full devices with the FA0.83CS0.17PbI3 absorber layer. The schematic n-i-p device architecture is shown in Figure 1a, using compact TiO2 as electron transport layer (ETL) and spiro-OMeTAD/ MoOx/ Au as hole transport layer (HTL) and metal electrode, respectively. We note that the additional processing steps in the device fabrication beyond the initial annealing step can have an impact on the level of mixing in the perovskite absorber layer. To avoid any changes in the nanoscale heterogeneity during the measurements, the temperatures during the WAXS experiments are kept below the initial annealing temperature.

Table 1. Overview of all tested annealing conditions with the respective sample IDs in "T_A-t_A" format, indicating which systems appeared well-mixed or heterogeneous. Blue backgrounds represent conditions that lead to a sharp tetragonal to cubic phase transition, green backgrounds represent conditions leading to a smeared phase transition. Grey background represents insufficiently high or long annealing conditions, leading to an incomplete conversion of precursor to perovskite.

Annealing Temperature (T _A) [°C]				
100	120	130	140	180

Annealing Time (t _A) [min]	15	100-15	120-15	130-15	140-15	180-15
	30		120-30	130-30	140-30	
	60	100-60	120-60	130-60		
	90		120-90	130-90		

For the structural part of our study, we use FA_{0.83}Cs_{0.17}PbI₃ perovskite thin films deposited on TiO₂-coated Silicon substrates (Fig. 1b). This aids the analysis because the characterization of the tetragonal to cubic phase transition is based on the t(210) superlattice peak ("t" indicates that we are using the tetragonal phase peak indexing and the numbers correspond to the relevant miller indices (hkl)), which has a low intensity (c.f. Fig. 1d). In Figure S2, we show exemplary data to demonstrate the reduction in intensity and disappearance of the t(210) peak across the tetragonal to cubic phase transition. When the structure is nearly cubic (i.e. presenting very small tilt angles/degree of tetragonality) the t(210) peak intensity will be low. Insufficient sensitivity in the diffraction measurements (i.e. the signal to noise ratio is small, impeding the detection of the t(210) superlattice peak associated with the tetragonal phase) can lead to a misjudgment of the actual phase transition temperature. However achieving a sufficient signal to noise ratio and collecting a few data points at temperatures across the phase transition suffices to classify the phase transition behavior into "sharp" or "smeared". Aspects of this were addressed by Barrier et al.³⁹. Typical glass/TCO substrates can further hamper the quantification of the t(210) peak intensity due to the superimposed background scattering from glass. By using Silicon substrates, the background scattering is reduced, improving the signal to noise ratio. By using Silicon substrates, the background scattering is reduced, improving the signal to noise ratio. The additional layer of TiO₂ was chosen to standardize the substrate formation surface and associated interfacial chemistry. This was done as the role of this lower interface on formation kinetics and defect structure for the metal halide perovskites is not well established and we strived to keep this as constant as possible.

For the sake of clarity, we will focus the main part of our discussion on a pair of samples and devices with different annealing times of the perovskite absorber layer, namely 15 ("140-15") and 30 ("140-30") minutes, at a moderate annealing temperature of 140°C. Following the initial discussion, results for additional annealing conditions will be presented.

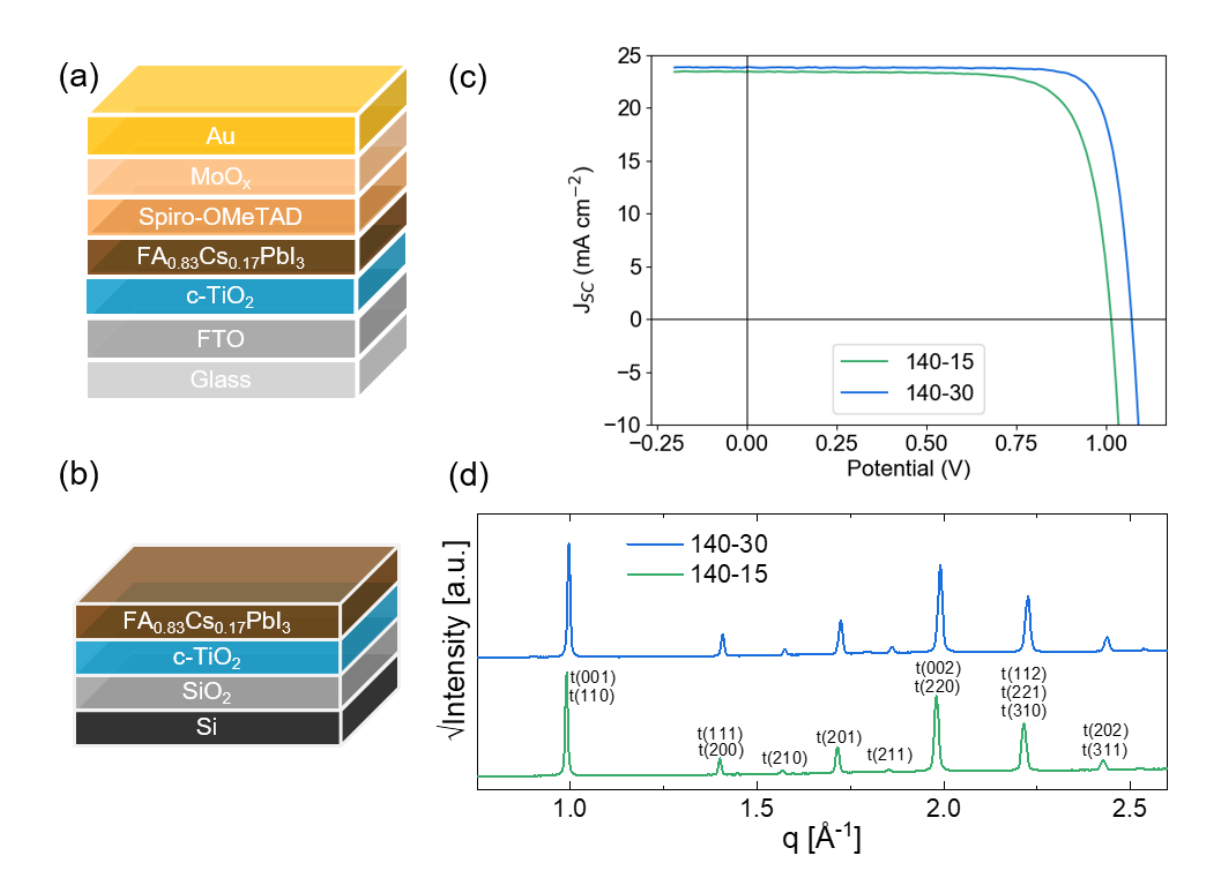


Figure 1. Schematic device stack used for performance and stability tests (a) and schematic layer stack of thin film configuration used for structural characterization (b). Current-voltage characteristics of two devices with different annealing times of the FA_{0.83}Cs_{0.17}PbI₃ absorber layer (c). XRD pattern indexed to the tetragonal phase as a function of the X-ray energy-independent scattering vector q ($q=4\pi/\lambda*\sin(2\Theta/2)$, with X-ray wavelength λ and scattering angle 2Θ) for corresponding, fully annealed thin film samples on Silicon substrates (d).

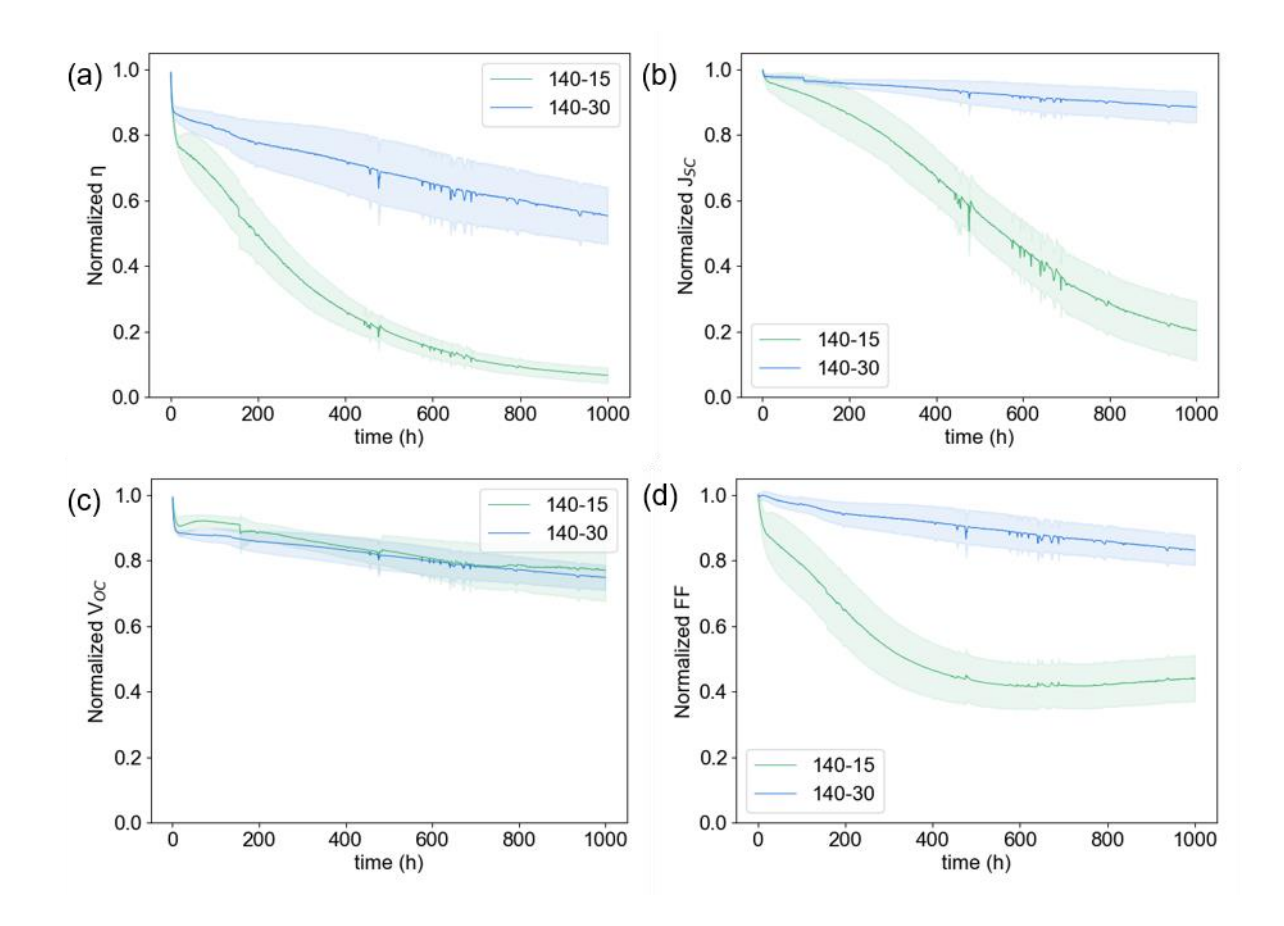


Figure 2. Device performance tracked over 1000h: The devices were kept under N_2 atmosphere at $33.2 \pm 0.7^{\circ}$ C and held under a resistive load of 510 Ohms, placing the cells near maximum power point. Power conversion efficiency η (a), short-circuit current J_{sc} (b), open-circuit voltage V_{oc} (c), and fill factor FF (d) for MHP devices with different annealing conditions used for the absorber layer. Plotted data show average over 6 (for 140-15) and 4 (for 140-30) devices per annealing condition as solid lines, shaded areas represent standard deviation. Superior performance stability can be observed for the longer annealed samples.

DEVICE STABILITY

Starting with the device characterization, we find the initial device performance for both devices (140-15, and 140-30) is reasonably high with 18.2% and 21%, respectively (Fig. 1c, Table 2). The current-voltage characteristics show a slightly higher open circuit voltage (V_{oc}) and fill factor (FF) in the case of the longer annealed sample. Notably, the short circuit current (J_{sc}) is nearly identical for both devices. Comparing the structural data of the two corresponding thin film samples, we find that the diffraction patterns reveal rather similar patterns (Fig. 1d).

Despite these similar electrical and structural characteristics in the initial state of the two thin films/ devices, a distinct difference in device performance stability over 1000 hours is found. To measure the stability, the devices were kept under N_2 atmosphere at approximately $33.2 \pm 0.7^{\circ}$ C (the temperature is calibrated on the absorber side of the device substrate) during the test and held under a resistive load of 510 Ohms, placing the cells near maximum power point. The conditions exclude the influence of oxygen, moisture and heat, enabling insights into intrinsic degradation mechanisms. Figure 2 shows the current-voltage parameters over time for an average over 6 (for 140-15) and 4 (for 140-30) analyzed devices: efficiency η (Fig. 2a), J_{sc} (Fig. 2b), V_{oc} (Fig. 2c) and FF (Fig. 2d). The data clearly shows that the shorter annealed sample 140-15 very quickly degrades and shows losses in all metrics, most severely in J_{sc} and FF. We note that both devices show significant losses in the V_{oc} , likely caused by burn-in effects as a result of the TiO₂ contact layer⁵¹. With all non-perovskite layers in the device deposited and processed identically, this result raises the question why one device completely degraded while the other showed a reasonable stability.

Table 2. Current-voltage parameters of champion devices for two annealing conditions: 140°C for 15 min ("140-15") and 140C for 30 min ("140-30"). Data based on reverse IV scans.

	140-15		140-30		
	initial	degraded	initial	degraded	
J _{sc} [mA/cm ²]	23.42	10.36	23.85	23.25	
V _{oc} [mV]	1.01	0.93	1.07	1.03	
FF	0.77	0.42	0.82	0.74	
η [%]	18.18	4.02	21.04	17.61	

A-SITE PHASE SEGREGATION

We hypothesize that the performance loss in the 140-15 samples is due to irreversible de-mixing and subsequent phase segregation, driven by the testing conditions and nucleated by a compositional heterogeneity on the nanoscale¹⁷. We further hypothesize that the level of this initial heterogeneity is larger in the case of the shorter annealed 140-15 samples, compared to the 140-30 samples. From the device stability measurements, we know that the longer annealed sample 140-30 shows superior stability. The degradation of the active layer in case of the shorter annealed sample 140-15 is even visible by eye, as photos of two degraded devices show in Figure 3b. While 140-30 shows no visible signs of degradation, the 140-15 device turned fully transparent on large parts of the substrate area. To investigate the structural stability and check for macroscale demixing and A-site phase segregation, we conducted synchrotron WAXS measurements on the degraded devices, probing the perovskite absorber layer through the top metal electrode. The structural analysis of the degraded devices reveals that irreversible phase changes into the photoinactive delta phases are causing the device performance degradation. Figure 3a shows the 140-30 azimuthally integrated 2D-WAXS data in blue (details of the integration limits can be found in the experimental section) together with reference patterns for the tetragonal perovskite phase (black),

FTO (orange), δ-phase of CsPbI₃ (bright red) and the δ-phase of FAPbI₃ (dark red). The scattering data reveal crystalline mixed A-site perovskite as the primary phase (marked with black cubes) with small contribution of the orthorhombic δ-phase of CsPbI₃ as seen from XRD peaks between 1.75 Å⁻¹ and 1.95 Å⁻¹ (marked with triangle). In addition, Bragg peaks corresponding to the FTO substrate are visible at 1.87 Å⁻¹ and 2.37 Å⁻¹ (marked with rhombus). The 140-15 data on the other hand, shown in green in Figure 3a, shows no contribution of the initial perovskite phase but rather exclusively the non-photo active δ-phases of FAPbI₃ (marked with star) and CsPbI₃ (marked with triangle). Based on the intensities, the hexagonal δ-phase of FAPbI₃ is the dominant phase, which is consistent with the significantly higher FA content in the initially mixed perovskite composition (FA:Cs = 83:17).

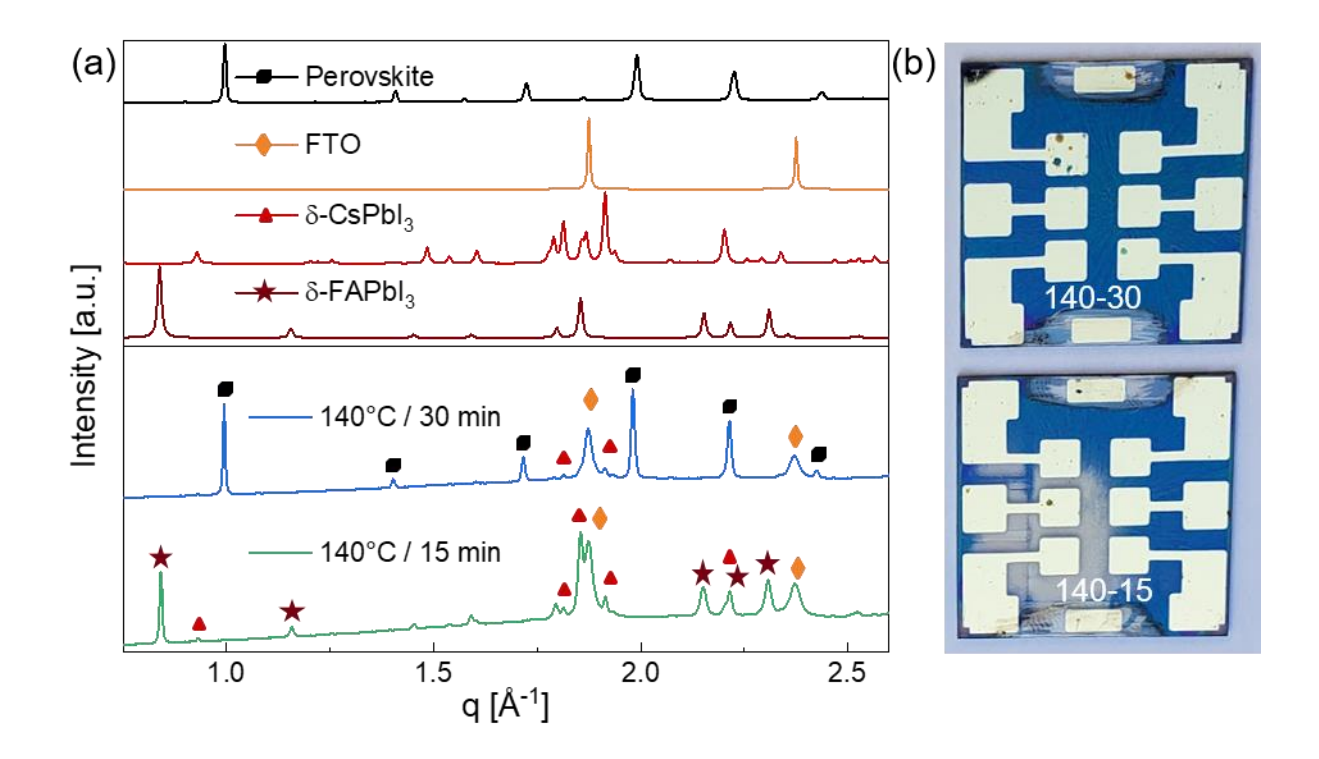


Figure 3. Degraded FA_{0.83}Cs_{0.17}PbI₃ devices after 1000h. XRD patterns of 140-15 (green), 140-30 (blue) as well as reference patterns for the tetragonal perovskite phase (black/cube), FTO (orange/ rhombus), δ-phase of CsPbI₃ (bright red/ triangle) and the δ-phase of FAPbI₃ (dark red/ star) (a) and photographs of 140-30 (top) and 140-15 (bottom) (b). The shorter annealed device shows visible degradation. Comparison with reference structures shows the decomposition in the δ-phases of CsPbI₃ and FAPbI₃. Additional reference structures include the mixed A-site perovskite phase and the substrate (FTO).

TETRAGONAL TO CUBIC PHASE TRANSITION BEHAVIOR

We further hypothesize that the observation of the operational induced de-mixing and the consequent A-site phase segregation and performance loss is nucleated by initial nanoscale heterogeneities. Therefore in this section we will focus on the analysis of nanoscale heterogeneity of the films prior to degradation using the technique introduced by Barrier et al.³⁹. As discussed briefly in the introduction, the technique is based on characterizing the tetragonal to cubic phase transition, schematically depicted in Figure 4. This phase transition is a reversible structural change that is distinct from the de-mixing and segregation into FA-/Cs-rich areas observed under operation or illumination. Figure S3 shows in situ XRD data during heating and cooling, demonstrating the reversible nature of the tetragonal to cubic phase transition as the tetragonal superlattice peaks fade during heating and emerge during cooling. The tetragonal phase of the perovskite is a distortion from the cubic lattice where the lead-iodide octahedra are tilted off axis from the cubic lattice. The tilt angle off the cubic lattice is defined here as the "degree of tetragonal distortion." When heated the tilt angle or "degree of tetragonality" is reduced until the system is fully cubic (Fig. 4). The tetragonal phase will have all the reflection from the cubic phase but because of a symmetry breaking, these will be split (generally to a degree not resolvable) and there will be additional

reflections (superlattice peaks). We determine the degree of tetragonality by comparing the intensity of one tetragonal superlattice peak and one peak that is also present in the cubic phase. The peak at 0.99 Å⁻¹ corresponds to the t(001)/t(110) reflection when indexed to the tetragonal phase (Fig. 1d), and to the c(100) reflection, when indexed to the cubic phase. The t(210) reflection at 1.57 Å⁻¹ is a superlattice peak and disappears during the tetragonal to cubic phase transition. The square root of the ratio between the intensities of these two peaks $\sqrt{I(t(210))/I(c(100))}$ is a measure for the degree of tetragonality. We define the transition temperature T_0 to be the temperature when the t(210) peak disappears, and we consider the system fully cubic³⁹. With this, we can determine the degree of tetragonality from the diffraction data.

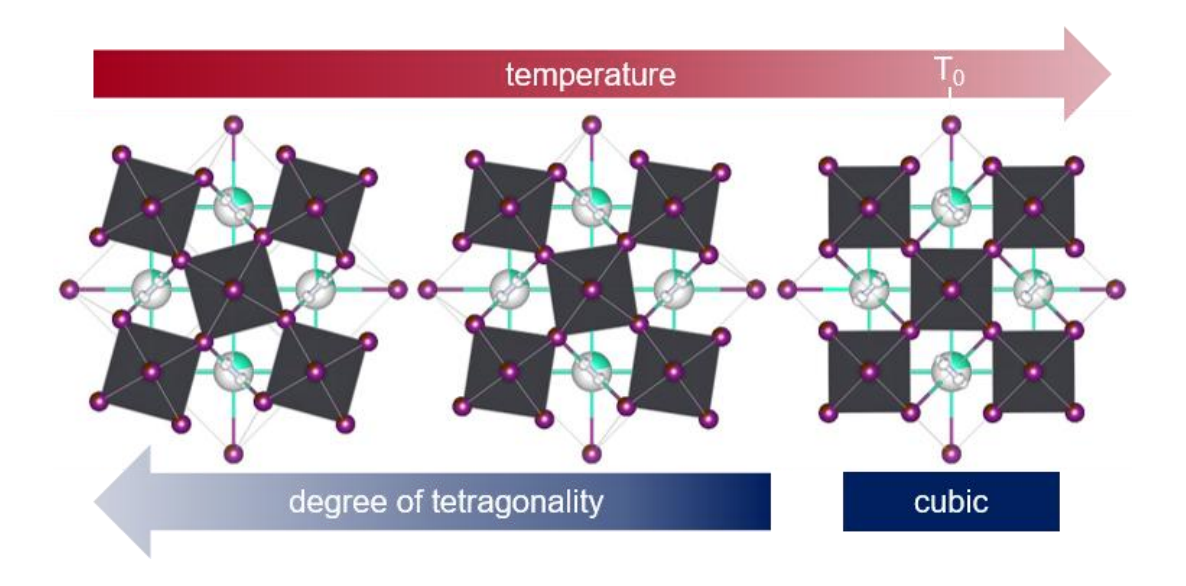


Figure 4. Schematic illustration of reduction of degree of tetragonality (left to right), which is proportional to the octahedral tilt angle off the cubic lattice, with increasing temperature. Transition temperature T₀, which is material specific, is here defined as the temperature when the degree of tetragonality is zero (cubic phase). Iodine atoms are represented in purple, the lead-iodine octahedra in dark gray. Cs/FA is depicted in light green/white, respectively.

Here we use the approach described above to determine the initial heterogeneity in fully annealed thin film samples synthesized at different annealing temperatures and annealing times as described in Table 1. The annealed films were slowly heated in 2°C steps from room temperature (RT) up to 140°C, taking WAXS data at every step. We found a strikingly different tetragonal to cubic phase transition behavior for the two annealing conditions; the results are shown in Figure 5. The waterfall plots (a,c) show the integrated in situ XRD patterns as a function of the scattering vector q, with increasing temperature on the y-axis and the color indicating the intensity. It can easily be seen that the tetragonal superlattice peak t(210) at 1.57 Å⁻¹ persists across a much larger temperature range for the shorter annealed sample, while the other peaks maintain their intensity, demonstrating that the tetragonal to cubic phase transition happens more gradually for the shorter annealed sample. We note that there are no other structural changes besides small shifts in the peak positions towards lower q caused by the thermal expansion of the lattice (corresponding to slightly larger lattice parameters). Specifically, no secondary phases from degradation products, such as lead iodide, emerge during the in situ heating experiment. An exemplary comparison of the XRD patterns close to RT and 135°C is shown for 140-30 in the SI (Fig. S4) to clearly demonstrate the absence of secondary phases due to thermal degradation or beam damage. Figure 5 (b,d) shows the degree of tetragonality as a function of temperature. As already seen from the waterfall plot, the two samples reach the cubic phase at very different temperatures. Both systems start at the same level of degree of tetragonality, however the tetragonal to cubic transition is far sharper for the longer annealed sample. The structure is fully cubic at 50°C for 140-30, while the shorter annealed sample 140-15 shows a smeared out tetragonal to cubic phase transition, reaching the cubic state close to 130°C.

It is evident that there are subtle structural differences caused by the difference in annealing conditions that cannot be detected by a single XRD measurement. From the work done by Barrier et al., we conclude that the smeared tetragonal to cubic phase transition is evidence for a higher level of nanoscale heterogeneity, as it represents a superposition of a range of compositions, which undergo the tetragonal to cubic phase transition at different phase transition temperatures. As shown in Figure 5, this means that there is a direct correlation between the thermal annealing conditions of the perovskite absorber layer and the resulting nanoscale heterogeneity. The finding that the nanoscale heterogeneity correlates with the thermal annealing conditions, further suggest that the heterogeneity can be mitigated by adapting optimal annealing conditions. In this case, we find that annealing longer will lead to a well-mixed state. Together with our findings about the device stability and the structural decomposition in the degraded devices, we conclude that the irreversible phase changes into the photo-inactive δ -phases (Fig. 3) are induced by compositional heterogeneity in the initial perovskite layer (Fig. 5). Thus, we have identified the structure-function relationship between the level of initial nanoscale compositional heterogeneity and device-level stability.

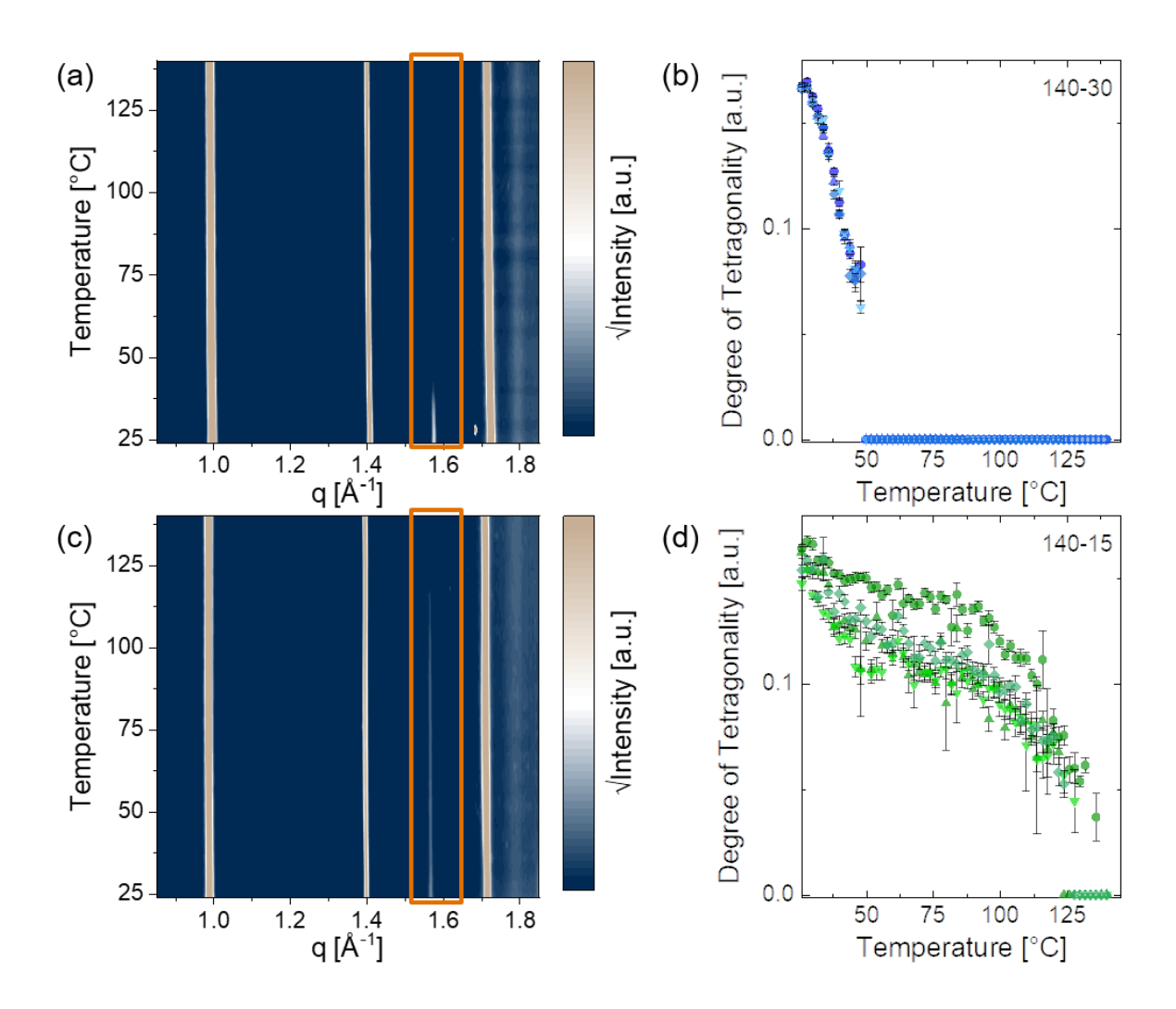


Figure 5. Temperature-dependent in situ XRD data from room temperature to 140°C for fully annealed MHP thin film samples on Silicon substrates synthesized with an annealing time of 30 min at 140°C (a-b) or 15 min at 140°C (c-d). Waterfall plots (a,c) with highlighted t(210) peak. Degree of tetragonality across the tetragonal to cubic phase transition, derived from the temperature-dependent WAXS measurements, showing a sharp (b) or smeared (d) phase transition, each plot shows the phase transition behavior for 4 repeat samples.

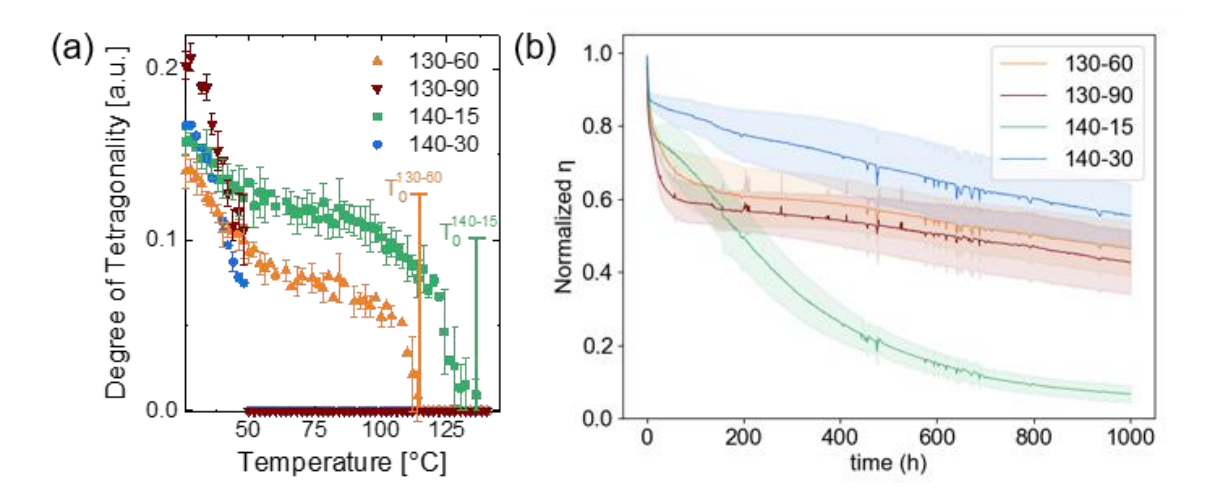


Figure 6. Degree of tetragonality across the tetragonal to cubic phase transition, derived from temperature-dependent WAXS measurements of fully annealed thin film samples synthesized at different annealing temperatures and annealing times: 140-15, 140-30, 130-60 and 130-90 (degree of tetragonality averaged over 4 repeat samples for each annealing condition) (a). Normalized power conversion efficiency η tracked over 1000 h for 140-15, 140-30, 130-60 and 130-90 (efficiency averaged over 6 (for 140-15 and 130-90) and 4 (for 140-30 and 130-60) devices). Solid lines represent averaged efficiency data, shaded areas represent standard deviation (b).

As mentioned earlier, we tested other conditions in addition to the two presented annealing conditions, varying both the annealing temperature and time (c.f. Table 1). We found that great care has to be taken when choosing annealing conditions to ensure full conversion of precursor to perovskite and also to ensure reproducibility as the nanoscale compositional heterogeneity is very sensitive to subtle changes in the processing conditions. Insufficient annealing can lead to residual precursors in the final thin film. Secondary phases, as shown in Figure S5 for 100-15, are a clear indicator for macroscale compositional heterogeneity, rather than the more subtle nanoscale local variations in composition we are looking to characterize. We conducted no further analysis on the samples showing residual precursor phases. The incomplete conversion in some samples further

highlights the pronounced process sensitivity of the compositional heterogeneity. In Table 1, all annealing conditions tested within this study are summarized, differentiating groups of wellmixed, heterogeneous, and not fully converted films. We find that at lower temperatures, the films require a significantly longer annealing time to reach a state without a measurable precursor phase present. We further find that reduced initial nanoscale heterogeneity, characterized by a sharp tetragonal to cubic phase transition, can be reached when annealing hotter, requiring a shorter annealing time, or with sufficiently long annealing time even at moderately low temperatures (Table 1 and Fig. S7). For the 130-60 and 130-90 samples specifically, we observe a sharp phase transition for an annealing time of 90 min (130-90) while after 60 min annealing the phase transition occurs over a larger temperature range (Fig. 6a). However, in the latter case, the phase transition behavior is still different from the stretched out phase transition for the 140-15 samples. The 130-60 samples reach the pure cubic phase at 115°C, showing a more narrow temperature range in which the phase transition occurs up to the indicated phase transition temperature (identified as T₀ in Fig. 6a). We propose that this suggests the 130-60 and 140-15 samples do not have the same level of nanoscale heterogeneity and that the 130-60 samples may be more mixed than the 140-15 samples.

When comparing the device stability of the 130-60 and 130-90 devices, a very similar trend is observed for both annealing times (Fig. 6b and Fig. S8a-d for all IV parameters). Similar results are also found for the post-stability testing XRD analysis of the devices, showing minor contributions from the δ -CsPbI₃ phase but not the severe, irreversible de-mixing and complete phase change into the δ -phases observed after operation for the 140-15 devices (Fig. S6). These observations suggest that there is a threshold for the degree of nanoscale heterogeneity to induce further A-site phase segregation. It is also feasible that the 130-60 devices would have segregated

into FA-/Cs-rich areas and changed into the pure δ -phases if run beyond 1000 hours as will be done in real operational conditions⁵². Previous work reporting calculations of the free Gibbs energy of mixing for FA_{1-x}Cs_xPbI₃ systems suggested that mixing in compositions with high Cs-contents >66% is thermodynamically unfavorable.¹⁷ Thus, if the nanoscale heterogeneity is sufficiently severe, it is likely to drive further phase segregation. This hypothesis is consistent with the observed higher transition temperature T₀ in the 140-15 sample compared to the 130-60 sample (temperature at which the system is fully cubic), since the pure CsPbI₃ perovskite has a higher tetragonal to cubic phase transition temperature than the pure FAPbI₃ perovskite.

A key takeaway from these observations is that heterogeneity is not binary but rather a continuum and this approach may be sensitive to varying degrees of heterogeneity. Determining a quantitative level of nanoscale heterogeneity will likely remain difficult and the extreme sensitivity to subtle modifications in the processing conditions resulting in micro-changes in the films and ultimately devices present challenges to this type of analysis. The sensitivity to the level of nanoscale heterogeneity in MHP to annealing temperature as well as time further emphasizes the need for careful process control to ensure reproducibility. This then lends merit to examinations of novel approaches to processes that can enable or otherwise ensure process reproducibility.

In conclusion, we find that monitoring the tetragonal to cubic phase transition behavior indirectly yields valuable insights into initial nanoscale compositional heterogeneity in mixed A-site MHPs. Further we show that a single XRD measurement cannot provide a complete picture of the structural properties in a system. Instead, we confirm that nanoscale compositional heterogeneity can indirectly be probed by measuring the cubic phase transition by in-situ X-ray scattering on

fully annealed films³⁹. This provides valuable insights into processing conditions and their reproducibility, by analyzing the width of the tetragonal to cubic phase transition. Heterogeneous films exhibit a phase transition that is smeared out over a large temperature range while wellmixed films exhibit a sharper phase transition. We show that initial nanoscale compositional heterogeneity in mixed A-site perovskites can be intentionally tuned and mitigated by adapting the thermal annealing conditions in the thin film processing. A well-mixed state can be reached for a sufficient thermal budget, i.e. annealing either long enough or hot enough. We further found evidence that in the presence of initial nanoscale compositional heterogeneity, the level strongly depends on the details of processing conditions. We highlight the significance of controlling initial nanoscale compositional heterogeneity as we find for these MHP materials it is correlated to performance stability. Device stability data over 1000 hours confirm that well-mixed films result in superior device stability, while under-annealed films with a high level of heterogeneity tend to de-mix and irreversibly segregate into FA-/Cs-rich areas during operation and subsequently form secondary, photo-inactive phases, leading to a severe loss in device performance. Thereby, we establish the structure-function relationship between initial nanoscale compositional heterogeneity and device stability. The insights generated in this study provide crucial information to guide manufacturing processes to enhance the stability of MHP solar cells.

ASSOCIATED CONTENT

Supporting Information. Experimental methods, Schematic to illustrate nanoscale compositional heterogeneity, exemplary XRD data showing the evolution of t(210) across the tetragonal to cubic

phase transition, comparison XRD pattern of tetragonal v. cubic phase, XRD pattern showing

residual precursor phase, XRD pattern for all degraded devices, summary of phase transition

behavior for all annealing conditions, device stability for 130-60 and 130-90, Table with I-V

characteristics for 130-60 and 130-90.

AUTHOR INFORMATION

Email: lmundt@slac.stanford.edu, Twitter: @lauraelenamundt

Email: michael.toney@colorado.edu, Twitter: @MMftoney

Email: <u>laura.schelhas@nrel.gov</u>, Twitter: @LSchelhas

Notes

The authors declare no competing financial interest.

ACKNOWLEDGMENT

This work was supported by the U.S. Department of Energy (DOE) Solar Energy Technology

Office (SETO) of the Energy Efficiency and Renewable Energy (EERE) award for the Derisking

Halide Perovskite Solar Cells project at the National Renewable Energy Laboratory under Contract

No. DE-AC36-08-GO28308 managed and operated by the Alliance for Sustainable Energy, LLC.

The use of the Stanford Synchrotron Radiation Lightsource, SLAC National Accelerator

Laboratory, is supported by the U.S. Department of Energy, Office of Science, Office of Basic

Energy Sciences under Contract No. DE-AC02-76SF00515. The views expressed in the article do

not necessarily represent the views of the DOE or the U.S. Government. The U.S. Government

retains and the publisher, by accepting the article for publication, acknowledges that the U.S.

Government retains a nonexclusive, paid-up, irrevocable, worldwide license to publish or

Pursuant to the DOE Public Access Plan, this document represents the authors' peer-reviewed, accepted manuscript. The published version of the article is available from the relevant publisher. 23

reproduce the published form of this work, or allow others to do so, for U.S. Government purposes. We thank Grace Suenram for assistance with figures.

REFERENCES

- (1) NREL Efficiency Chart. https://www.nrel.gov/pv/cell-efficiency.html (accessed December 23, 2021)
- (2) Eperon, G. E.; Stranks, S. D.; Menelaou, C.; Johnston, M. B.; Herz, L. M.; Snaith, H. J. Formamidinium Lead Trihalide: A Broadly Tunable Perovskite for Efficient Planar Heterojunction Solar Cells. *Energy Environ. Sci.* 2014, 7 (3), 982–988. https://doi.org/10.1039/c3ee43822h.
- (3) McMeekin, D. P.; Sadoughi, G.; Rehman, W.; Eperon, G. E.; Saliba, M.; Hörantner, M. T.; Haghighirad, A.; Sakai, N.; Korte, L.; Rech, B.; Johnston, M. B.; Herz, L. M.; Snaith, H. J. A Mixed-Cation Lead Mixed-Halide Perovskite Absorber for Tandem Solar Cells. *Science* (80-.). 2016, 351 (6269), 151–155. https://doi.org/10.1126/science.aad5845.
- (4) Prasanna, R.; Gold-Parker, A.; Leijtens, T.; Conings, B.; Babayigit, A.; Boyen, H. G.; Toney, M. F.; McGehee, M. D. Band Gap Tuning via Lattice Contraction and Octahedral Tilting in Perovskite Materials for Photovoltaics. *J. Am. Chem. Soc.* 2017, 139 (32), 11117–11124. https://doi.org/10.1021/jacs.7b04981.
- (5) Eperon, G. E.; Stone, K. H.; Mundt, L. E.; Schloemer, T. H.; Habisreutinger, S. N.; Dunfield, S. P.; Schelhas, L. T.; Berry, J. J.; Moore, D. T.; Eperon, G. E.; Moore, D. T. The Role of Dimethylammonium in Bandgap Modulation for Stable Halide Perovskites. *ACS Energy Lett.* 2020, 5 (6), 1856–1864. https://doi.org/10.1021/acsenergylett.0c00872.

- (6) Jeon, N. J.; Noh, J. H.; Yang, W. S.; Kim, Y. C.; Ryu, S.; Seo, J.; Seok, S. Il. Compositional Engineering of Perovskite Materials for High-Performance Solar Cells. *Nature* 2015, 517 (7535), 476–480. https://doi.org/10.1038/nature14133.
- (7) Jesper Jacobsson, T.; Correa-Baena, J. P.; Pazoki, M.; Saliba, M.; Schenk, K.; Grätzel, M.; Hagfeldt, A. Exploration of the Compositional Space for Mixed Lead Halogen Perovskites for High Efficiency Solar Cells. *Energy Environ. Sci.* 2016, 9 (5), 1706–1724. https://doi.org/10.1039/c6ee00030d.
- (8) Zarick, H. F.; Soetan, N.; Erwin, W. R.; Bardhan, R. Mixed Halide Hybrid Perovskites: A Paradigm Shift in Photovoltaics. J. Mater. Chem. A 2018, 6 (14), 5507–5537. https://doi.org/10.1039/c7ta09122b.
- (9) Ono, L. K.; Juarez-Perez, E. J.; Qi, Y. Progress on Perovskite Materials and Solar Cells with Mixed Cations and Halide Anions. ACS Appl. Mater. Interfaces 2017, 9 (36), 30197–30246. https://doi.org/10.1021/acsami.7b06001.
- (10) Leblanc, A.; Mercier, N.; Allain, M.; Dittmer, J.; Pauporté, T.; Fernandez, V.; Boucher, F.;
 Kepenekian, M.; Katan, C. Enhanced Stability and Band Gap Tuning of α-[HC(NH2)2]PbI3
 Hybrid Perovskite by Large Cation Integration. ACS Appl. Mater. Interfaces 2019, 11 (23),
 20743–20751. https://doi.org/10.1021/acsami.9b00210.
- (11) Li, Z.; Yang, M.; Park, J. S.; Wei, S. H.; Berry, J. J.; Zhu, K. Stabilizing Perovskite Structures by Tuning Tolerance Factor: Formation of Formamidinium and Cesium Lead Iodide Solid-State Alloys. *Chem. Mater.* 2016, 28 (1), 284–292. https://doi.org/10.1021/acs.chemmater.5b04107.

- (12) Saliba, M.; Matsui, T.; Seo, J. Y.; Domanski, K.; Correa-Baena, J. P.; Nazeeruddin, M. K.; Zakeeruddin, S. M.; Tress, W.; Abate, A.; Hagfeldt, A.; Grätzel, M. Cesium-Containing Triple Cation Perovskite Solar Cells: Improved Stability, Reproducibility and High Efficiency. *Energy Environ. Sci.* 2016, 9 (6), 1989–1997. https://doi.org/10.1039/c5ee03874j.
- (13) Lee, J. W.; Kim, D. H.; Kim, H. S.; Seo, S. W.; Cho, S. M.; Park, N. G. Formamidinium and Cesium Hybridization for Photo- and Moisture-Stable Perovskite Solar Cell. *Adv. Energy Mater.* **2015**, *5* (20). https://doi.org/10.1002/aenm.201501310.
- (14) Salado, M.; Kazim, S.; Ahmad, S. The Role of Cs+ Inclusion in Formamidinium Lead Triiodide-Based Perovskite Solar Cell. *Chem. Pap.* **2018**, 72 (7), 1645–1650. https://doi.org/10.1007/s11696-017-0373-7.
- (15) Sun, S.; Tiihonen, A.; Oviedo, F.; Liu, Z.; Thapa, J.; Zhao, Y.; Hartono, N. T. P.; Goyal, A.; Heumueller, T.; Batali, C.; Encinas, A.; Yoo, J. J.; Li, R.; Ren, Z.; Peters, I. M.; Brabec, C. J.; Bawendi, M. G.; Stevanovic, V.; Fisher, J.; Buonassisi, T. A Data Fusion Approach to Optimize Compositional Stability of Halide Perovskites. *Matter* 2021, 4 (4), 1305–1322. https://doi.org/10.1016/j.matt.2021.01.008.
- (16) Goldschmidt, V. M. Die Gesetze Der Krystallochemie. *Naturwissenschaften* **1926**, *14*, 477–485.
- (17) Schelhas, L. T.; Li, Z.; Christians, J. A.; Goyal, A.; Kairys, P.; Harvey, S. P.; Kim, D. H.; Stone, K. H.; Luther, J. M.; Zhu, K.; Stevanovic, V.; Berry, J. J. Insights into Operational Stability and Processing of Halide Perovskite Active Layers. *Energy Environ. Sci.* **2019**, *12*

- (4), 1341–1348. https://doi.org/10.1039/c8ee03051k.
- (18) Li, N.; Luo, Y.; Chen, Z.; Niu, X.; Zhang, X.; Lu, J.; Kumar, R.; Jiang, J.; Liu, H.; Guo, X.; Lai, B.; Brocks, G.; Chen, Q.; Tao, S.; Fenning, D. P.; Zhou, H. Microscopic Degradation in Formamidinium-Cesium Lead Iodide Perovskite Solar Cells under Operational Stressors.

 Joule 2020, 4 (8), 1743–1758. https://doi.org/10.1016/j.joule.2020.06.005.
- (19) Beal, R. E.; Zhou Hagström, N.; Barrier, J.; Gold-Parker, A.; Prasanna, R.; Bush, K. A.; Passarello, D.; Schelhas, L. T.; Brüning, K.; Tassone, C. J.; Steinrück, H.-G.; McGehee, M. D.; Toney, M. F.; Nogueira, A. F. Structural Origins of Light-Induced Phase Segregation in Organic-Inorganic Halide Perovskite Photovoltaic Materials. *Matter* 2019, 01, 207–219. https://doi.org/10.1016/j.matt.2019.11.001.
- (20) Knight, A. J.; Borchert, J.; Oliver, R. D. J.; Patel, J. B.; Radaelli, P. G.; Snaith, H. J.; Johnston, M. B.; Herz, L. M. Halide Segregation in Mixed-Halide Perovskites: In Fl Uence of A Site Cations. ACS Energy Lett. 2021, 6 (2), 799–808. https://doi.org/10.1021/acsenergylett.0c02475.
- (21) Tang, X.; Van Den Berg, M.; Gu, E.; Horneber, A.; Matt, G. J.; Osvet, A.; Meixner, A. J.; Zhang, D.; Brabec, C. J. Local Observation of Phase Segregation in Mixed-Halide Perovskite. Nano Lett. 2018, 18 (3), 2172–2178. https://doi.org/10.1021/acs.nanolett.8b00505.
- Hoke, E. T.; Slotcavage, D. J.; Dohner, E. R.; Bowring, A. R.; Karunadasa, H. I.; McGehee,
 M. D. Reversible Photo-Induced Trap Formation in Mixed-Halide Hybrid Perovskites for
 Photovoltaics. *Chem. Sci.* 2015, 6 (1), 613–617. https://doi.org/10.1039/c4sc03141e.

- (23) Knight, A. J.; Herz, L. M. Preventing Phase Segregation in Mixed-Halide Perovskites: A Perspective. *Energy Environ. Sci.* **2020**, *13* (7), 2024–2046. https://doi.org/10.1039/d0ee00788a.
- (24) Ali, A.; Park, H.; Mall, R.; Aïssa, B.; Sanvito, S.; Bensmail, H.; Belaidi, A.; El-Mellouhi, F. Machine Learning Accelerated Recovery of the Cubic Structure in Mixed-Cation Perovskite Thin Films. *Chem. Mater.* **2020**, *32* (7), 2998–3006. https://doi.org/10.1021/acs.chemmater.9b05342.
- (25) Stoumpos, C. C.; Malliakas, C. D.; Kanatzidis, M. G. Semiconducting Tin and Lead Iodide Perovskites with Organic Cations: Phase Transitions, High Mobilities, and near-Infrared Photoluminescent Properties. *Inorg. Chem.* 2013, 52 (15), 9019–9038. https://doi.org/10.1021/ic401215x.
- (26) An, Y.; Hidalgo, J.; Perini, C. A. R.; Castro-Méndez, A. F.; Vagott, J. N.; Bairley, K.; Wang, S.; Li, X.; Correa-Baena, J. P. Structural Stability of Formamidinium- And Cesium-Based Halide Perovskites. ACS Energy Lett. 2021, 6 (5), 1942–1969. https://doi.org/10.1021/acsenergylett.1c00354.
- (27) DeQuilettes, D. W.; Zhang, W.; Burlakov, V. M.; Graham, D. J.; Leijtens, T.; Osherov, A.; Bulović, V.; Snaith, H. J.; Ginger, D. S.; Stranks, S. D. Photo-Induced Halide Redistribution in Organic-Inorganic Perovskite Films. *Nat. Commun.* **2016**, 7 (May). https://doi.org/10.1038/ncomms11683.
- (28) Braunger, S.; Mundt, L. E.; Wolff, C. M.; Mews, M.; Rehermann, C.; Jošt, M.; Tejada, A.; Eisenhauer, D.; Becker, C.; Guerra, J. A.; Unger, E.; Korte, L.; Neher, D.; Schubert, M. C.;

- Rech, B.; Albrecht, S. CsxFA1- XPb(I1- YBry)3 Perovskite Compositions: The Appearance of Wrinkled Morphology and Its Impact on Solar Cell Performance. *J. Phys. Chem. C* **2018**, *122* (30). https://doi.org/10.1021/acs.jpcc.8b06459.
- (29) Mundt, L. E.; Kwapil, W.; Yakoob, M. A.; Herterich, J. P.; Kohlstadt, M.; Wurfel, U.; Schubert, M. C.; Glunz, S. W. Quantitative Local Loss Analysis of Blade-Coated Perovskite Solar Cells. *IEEE J. Photovoltaics* 2019, 9 (2). https://doi.org/10.1109/JPHOTOV.2018.2888835.
- (30) Moerman, D.; Eperon, G. E.; Precht, J. T.; Ginger, D. S. Correlating Photoluminescence Heterogeneity with Local Electronic Properties in Methylammonium Lead Tribromide Perovskite Thin Films. *Chem. Mater.* 2017, 29 (13), 5484–5492. https://doi.org/10.1021/acs.chemmater.7b00235.
- (31) Eperon, G. E.; Moerman, D.; Ginger, D. S. Anticorrelation between Local Photoluminescence and Photocurrent Suggests Variability in Contact to Active Layer in Perovskite Solar Cells. *ACS Nano* **2016**, *10* (11), 10258–10266. https://doi.org/10.1021/acsnano.6b05825.
- (32) Jones, T. W.; Osherov, A.; Alsari, M.; Sponseller, M.; Duck, B. C.; Jung, Y. K.; Settens, C.; Niroui, F.; Brenes, R.; Stan, C. V.; Li, Y.; Abdi-Jalebi, M.; Tamura, N.; MacDonald, J. E.; Burghammer, M.; Friend, R. H.; Bulović, V.; Walsh, A.; Wilson, G. J.; Lilliu, S.; Stranks, S. D. Lattice Strain Causes Non-Radiative Losses in Halide Perovskites. *Energy Environ. Sci.* 2019, 12 (2), 596–606. https://doi.org/10.1039/c8ee02751j.
- (33) Bischak, C. G.; Sanehira, E. M.; Precht, J. T.; Luther, J. M.; Ginsberg, N. S. Heterogeneous

- Charge Carrier Dynamics in Organic-Inorganic Hybrid Materials: Nanoscale Lateral and Depth-Dependent Variation of Recombination Rates in Methylammonium Lead Halide Perovskite Thin Films. *Nano Lett.* **2015**, *15* (7), 4799–4807. https://doi.org/10.1021/acs.nanolett.5b01917.
- (34) Bischak, C. G.; Hetherington, C. L.; Wu, H.; Aloni, S.; Ogletree, D. F.; Limmer, D. T.; Ginsberg, N. S. Origin of Reversible Photoinduced Phase Separation in Hybrid Perovskites.

 Nano Lett. 2017, 17 (2), 1028–1033. https://doi.org/10.1021/acs.nanolett.6b04453.
- (35) Bischak, C. G.; Wong, A. B.; Lin, E.; Limmer, D. T.; Yang, P.; Ginsberg, N. S. Tunable Polaron Distortions Control the Extent of Halide Demixing in Lead Halide Perovskites. *J. Phys. Chem. Lett.* **2018**, *9* (14), 3998–4005. https://doi.org/10.1021/acs.jpclett.8b01512.
- (36) Suchan, K.; Merdasa, A.; Rehermann, C.; Unger, E. L.; Scheblykin, I. G. Complex Evolution of Photoluminescence during Phase Segregation of MAPb(I1-XBrx)3 Mixed Halide Perovskite. *J. Lumin.* 2020, 221 (August 2019), 117073. https://doi.org/10.1016/j.jlumin.2020.117073.
- (37) Rehermann, C.; Merdasa, A.; Suchan, K.; Schröder, V.; Mathies, F.; Unger, E. L. Origin of Ionic Inhomogeneity in MAPb(IxBr1-x)3Perovskite Thin Films Revealed by In-Situ Spectroscopy during Spin Coating and Annealing. ACS Appl. Mater. Interfaces 2020, 12 (27), 30343–30352. https://doi.org/10.1021/acsami.0c05894.
- (38) Tiede, D. O.; Calvo, M. E.; Galisteo-López, J. F.; Míguez, H. Local Rearrangement of the Iodide Defect Structure Determines the Phase Segregation Effect in Mixed-Halide Perovskites. *J. Phys. Chem. Lett.* **2020**, *11* (12), 4911–4916.

- https://doi.org/10.1021/acs.jpclett.0c01127.
- (39) Barrier, J.; Beal, R. E.; Gold-Parker, A.; Vigil, J. A.; Wolf, E.; Waquier, L.; Weadock, N. J.; Zhang, Z.; Schelhas, L. T.; Nogueira, A. F.; McGehee, M. D.; Toney, M. F. Compositional Heterogeneity in CsyFA1–YPb(BrxI1–x)3 Perovskite Films and Its Impact on Phase Behavior. *Energy Environ. Sci.* 2021, Accepted Manuscript. https://doi.org/DOI https://doi.org/10.1039/D1EE01184G.
- (40) Hidalgo, J.; Castro-Méndez, A. F.; Correa-Baena, J. P. Imaging and Mapping Characterization Tools for Perovskite Solar Cells. *Adv. Energy Mater.* **2019**, *1900444*, 1–30. https://doi.org/10.1002/aenm.201900444.
- (41) Hoye, R. L. Z.; Schulz, P.; Schelhas, L. T.; Holder, A. M.; Stone, K. H.; Perkins, J. D.; Vigil-Fowler, D.; Siol, S.; Scanlon, D. O.; Zakutayev, A.; Walsh, A.; Smith, I. C.; Melot, B. C.; Kurchin, R. C.; Wang, Y.; Shi, J.; Marques, F. C.; Berry, J. J.; Tumas, W.; Lany, S.; Stevanović, V.; Toney, M. F.; Buonassisi, T. Perovskite-Inspired Photovoltaic Materials: Toward Best Practices in Materials Characterization and Calculations. *Chem. Mater.* 2017, 29 (5), 1964–1988. https://doi.org/10.1021/acs.chemmater.6b03852.
- (42) Chen, S.; Zhang, X.; Zhao, J.; Zhang, Y.; Kong, G.; Li, Q.; Li, N.; Yu, Y.; Xu, N.; Zhang, J.; Liu, K.; Zhao, Q.; Cao, J.; Feng, J.; Li, X.; Qi, J.; Yu, D.; Li, J.; Gao, P. Atomic Scale Insights into Structure Instability and Decomposition Pathway of Methylammonium Lead Iodide Perovskite. *Nat. Commun.* 2018, 9 (1), 1–8. https://doi.org/10.1038/s41467-018-07177-y.
- (43) Kosar, S.; Winchester, A. J.; Doherty, T. A. S.; Macpherson, S.; Petoukhoff, C. E.; Frohna,

- K.; Anaya, M.; Chan, N. S.; Madéo, J.; Man, M. K. L.; Stranks, S. D.; Dani, K. M. Unraveling the Varied Nature and Roles of Defects in Hybrid Halide Perovskites with Time-Resolved Photoemission Electron Microscopy. **2021**. https://doi.org/10.1039/d1ee02055b.
- (44) Doherty, T. A. S.; Winchester, A. J.; Macpherson, S.; Johnstone, D. N.; Pareek, V.; Tennyson, E. M.; Kosar, S.; Kosasih, F. U.; Anaya, M.; Abdi-Jalebi, M.; Andaji-Garmaroudi, Z.; Wong, E. L.; Madéo, J.; Chiang, Y. H.; Park, J. S.; Jung, Y. K.; Petoukhoff, C. E.; Divitini, G.; Man, M. K. L.; Ducati, C.; Walsh, A.; Midgley, P. A.; Dani, K. M.; Stranks, S. D. Performance-Limiting Nanoscale Trap Clusters at Grain Junctions in Halide Perovskites. *Nature* 2020, 580 (7803), 360–366. https://doi.org/10.1038/s41586-020-2184-1.
- (45) Szostak, R.; Silva, J. C.; Turren-Cruz, S. H.; Soares, M. M.; Freitas, R. O.; Hagfeldt, A.; Tolentino, H. C. N.; Nogueira, A. F. Nanoscale Mapping of Chemical Composition in Organic-Inorganic Hybrid Perovskite Films. *Sci. Adv.* 2019, 5 (10), 2–9. https://doi.org/10.1126/sciadv.aaw6619.
- (46) Nishida, J.; Alfaifi, A. H.; Gray, T. P.; Shaheen, S. E.; Raschke, M. B. Heterogeneous Cation–Lattice Interaction and Dynamics in Triple-Cation Perovskites Revealed by Infrared Vibrational Nanoscopy. ACS Energy Lett. 2020, 5 (5), 1636–1643. https://doi.org/10.1021/acsenergylett.0c00522.
- (47) Li, J.; Huang, B.; Nasr Esfahani, E.; Wei, L.; Yao, J.; Zhao, J.; Chen, W. Touching Is Believing: Interrogating Halide Perovskite Solar Cells at the Nanoscale via Scanning Probe Microscopy /639/925/930/328 /639/301/299/946 /639/4077/909 /639/301/119/996 Perspective. npj Quantum Mater. 2017, 2 (1). https://doi.org/10.1038/s41535-017-0061-4.

- (48) Wang, Y.; Hu, Z.; Gao, C.; Yang, C.; Zhang, J.; Zhu, Y. Comprehensive Elucidation of Grain Boundary Behavior in All-Inorganic Halide Perovskites by Scanning Probe Microscopy. Adv. Mater. Interfaces 2020, 7 (7), 1–8. https://doi.org/10.1002/admi.201901521.
- (49) Bu, T.; Li, J.; Li, H.; Tian, C.; Su, J.; Tong, G.; Ono, L. K.; Wang, C.; Lin, Z.; Chai, N.; Zhang, X. L.; Chang, J.; Lu, J.; Zhong, J.; Huang, W.; Qi, Y.; Cheng, Y. B.; Huang, F. Lead Halide-Templated Crystallization of Methylamine-Free Perovskite for Efficient Photovoltaic Modules. *Science* (80-.). **2021**, 372 (6548), 1327–1332. https://doi.org/10.1126/science.abh1035.
- (50) Gao, X. X.; Luo, W.; Zhang, Y.; Hu, R.; Zhang, B.; Züttel, A.; Feng, Y.; Nazeeruddin, M.
 K. Stable and High-Efficiency Methylammonium-Free Perovskite Solar Cells. *Adv. Mater.*2020, 32 (9), 1–9. https://doi.org/10.1002/adma.201905502.
- (51) Christians, J. A.; Schulz, P.; Tinkham, J. S.; Schloemer, T. H.; Harvey, S. P.; Tremolet De Villers, B. J.; Sellinger, A.; Berry, J. J.; Luther, J. M. Tailored Interfaces of Unencapsulated Perovskite Solar Cells for >1,000 Hour Operational Stability. *Nat. Energy* **2018**, *3* (1), 68–74. https://doi.org/10.1038/s41560-017-0067-y.
- (52) Li, N.; Niu, X.; Li, L.; Wang, H.; Huang, Z.; Zhang, Y.; Chen, Y.; Zhang, X.; Zhu, C.; Zai, H.; Bai, Y.; Ma, S.; Liu, H.; Liu, X.; Guo, Z.; Liu, G.; Fan, R.; Chen, H.; Wang, J.; Lun, Y.; Wang, X.; Hong, J.; Xie, H.; Jakob, D. S.; Xu, X. G.; Chen, Q.; Zhou, H. Liquid Medium Annealing for Fabricating Durable Perovskite Solar Cells with Improved Reproducibility. *Science (80-.)* 2021, 373 (6554), 561–567. https://doi.org/10.1126/science.abh3884.